Journal of Mechanical Science and Technology 34 (11) 2020

Original Article
DOI 10.1007/s12206-020-0703-5

Keywords:
· Dynamics
· Field vibration test
· Multi-degree of freedom dynamic model
· Vibration absorption structure
· Vibration characteristics
· TBM

Correspondence to:
Hanyang Wu
wuhanyang@mail.dlut.edu.cn

Citation:
Huo, J., Wu, H., Ji, W. (2020). Anti-vibration design for TBM main drive system based on multi-directional coupling dynamic characteristics analysis. Journal of Mechanical Science and Technology 34 (11) (2020) 4405~4421.
http://doi.org/10.1007/s12206-020-0703-5

Received January 9th, 2020
Revised April 17th, 2020
Accepted May 18th, 2020

† Recommended by Editor
No-cheol Park

Anti-vibration design for TBM main drive system based on multi-directional coupling dynamic characteristics analysis

Junzhou Huo, Hanyang Wu and Wenbo Ji

School of Mechanical Engineering, Dalian University of Technology, Dalian 116024, China

Abstract Extreme vibration often occurs on TBM main system during the tunneling process. This paper established the mathematical model for TBM main system considering the impact load, time-varying internal incentive and the complex coupling relationship between each vibration degree of freedom. The dynamic model was modified by the multi-point vibration measured data. The calculation error of the system response of the main support frame's main vibration direction was within 10 %. And it was found that the overturning vibration and axial vibration of the system were the main forms of vibration of the system. It was determined that the low-frequency vibration of 15-20 Hz was a coupled vibration of system's first to fourth mode vibration mode. Based on the vibration characteristics of TBM main system, this paper designed a tuned mass vibration absorption structure (TMVAS) that can adapt to the multi degree of freedom (MDOF) coupling vibration of TBM main system during the actual tunneling process. To minimize system vibration, the optimal design parameters of the system was determined. The maximum amplitude of the axial and horizontal overturning vibration of the support frame was reduced by 26.7 % and 13 %, and the maximum amplitude of the cutterhead's axial vibration was reduced by 23.2 %.

1. Introduction

The hard rock tunneling boring machine (TBM) is a large-scale complex equipment with tunneling, drainage, support and other functions. The TBM main drive system is the core component of the TBM. Its key components include main bearings, drive gear, motors and reducers. At the same time, a large number of hydraulic lines and control components are installed inside the main drive system. In the actual excavation process, the front end of the cutter head will encounter high-hardness rock. Due to the way the cutter breaks the rock, the TBM main drive system will be subjected to strong impact loads, resulting in extremely severe vibration of the machine. This directly affects the stability, life and tunneling performance of the TBM. In severe cases, it will cause serious engineering problems in the key components of the TBM system.

The basis of TBM vibration reduction design is to study the dynamic characteristics of the TBM main system. Meanwhile the basis of the research on the dynamic characteristics of the system is the study of the external load. The cutter rock breaking experiment is one of the most effective methods to accurately obtain the dynamic rock breaking load of the cutter under different excavation conditions. Scholars of Colorado School of Mines [1] established a cutter load prediction model based on cutter rock breaking test, this model was widely used at present. Entacher [2] designed a high-precision cutter rock-breaking scale test bench, obtained the time-domain load curve of the cutter under different surrounding rock, and proposed the corresponding prediction model of the cutter force. Xia [3, 4] established a multi-cutter rotary cutting test bench, and carried out the combined rock breaking experiment of the cutter group, and obtained the rock breaking load of the cutter in different positions of cutterhead under the experimental conditions. Entacher et al. [5, 6] placed the strain gauge system near the cutter-shaft at different positions on the cutter head based on the Koralm tunnel, so as to obtain the actual load of the cutter at different positions of the cutterhead. The cutter load increased with the diameter of the cutterhead. This conclusion provided a basis for synthesizing the cutterhead load. Some scholars [7-10] described the constitutive relationship of rock based on experiments, and simulated the process of cutter-rock breaking progress based on finite element method, and obtained the dynamic three-dimensional load. This numerical simulation method can be used to calculate the rock breaking load of cutter under different cutting conditions such as installation angle and penetration. For the dynamic characteristics of the main system, at present, most scholars analyzed the dynamic characteristics of the system based on the dynamics model of TBM system. Based on the study of dynamic characteristics, the design parameters and the excavation parameters were redesigned to improve anti-vibration ability of the main system, thereby reducing the vibration of the TBM system. Sun et al. [11] considered the multi- drive source of the cutterhead system, established the multi degree of freedom coupling dynamic model of the system, and analyzed the dynamic characteristics of the cutterhead system. Based on this model, Wei et al. [12] considered the drive system's reducer to improve the model’s accuracy, and the centralized mass method and the finite element method were combined to model the system. Based on this model, the dynamic characteristics of the drive system were further studied and analyzed. Huo et al. [13, 14] conducted field tests to test the vibration at the front end of the TBM main system. The main drive system dynamics model was modified based on field measured data. Based on the dynamic model, the mass of cutter head center block, the gear shaft length and other design parameters were designed for vibration resistance. Zou et al. [15] established the dynamic model for TBM support propulsion system considering the translational freedom of the system. Based on the field engineering, the vibration of the main beam was measured and compared with the theoretical calculation. The vibration energy of the system under different penetration and rock types was studied. Chen et al. [16, 17] presented a dynamic model for TBM gripping thrusting system considering surrounding rock boundary condition and configuration-dependent rigidities of the actuators, the vibration energy distribution was predicted and the vibration condition of the system under various typical working conditions was analyzed. In short, for the study of TBM vibration control, most scholars studied the vibration characteristics and vibration transmission laws of the system based on the dynamic model. Based on this, the key support parts of the system were determined, and the vibration reduction design was carried out by increasing the support stiffness at these parts. But in the actual manufacturing process, the effective support stiffness of key parts of the system will not been effectively increased by increasing the size of the support structure. This design not only failed to effectively reduce vibration, but also significantly reduced the tunneling efficiency of the machine. On the other hand, scholars used active vibration control to reduce the problem of extreme vibration encountered during actual tunneling. Vogiatzis et al. [18] installed a vibration real-time monitoring system on the machine based on the actual tunneling project, and actively adjusted the tunneling rate when the vibration level was too large. Buckley [19] installed a series of vibration sensors near the cutterhead of TBM to monitor the vibration level of the system during the actual tunneling process. The vibration signal based on real-time feedback adjusts the operating parameters of the machine to ensure the safety of the system through the tunnel fracture zone. However, this method of controlling the tunneling parameters with the actual vibration signal as the feedback signal means significantly the tunneling efficiency decrease. For low-frequency and high-amplitude vibration, tuned mass damper (TMD) has a good vibration reduction effect, so it has been widely used in the vibration reduction of high-rigidity systems such as bridges, high buildings and ocean platform [20-23]. A large number of studies have found that a well-designed TMD system can achieve a vibration absorption effect of about 30 %, which can significantly reduce the vibration level of the structure [24]. However, for large system, the TMD system requires a large mass object to absorb system vibration. At the same time, the traditional TMD system often targets the single-direction vibration of the system. When the system is in a state of multi degree of freedom coupled vibration, the damping effect of the traditional TMD system is poor.

This paper aims to apply tuned mass damping theory to the TBM main system, and a vibration conduction structure adapted to the multi-degree-of-freedom coupled vibration of the main system during the actual tunneling process is designed. Based on the structure of the vibration absorption system, the dynamic model is established. The calculation results of the theoretical model are modified and verified based on the field vibration test and the cutter rock breaking experiment. The main vibration frequency band of the main structure is determined. The main parameters of the vibration absorption system are designed based on dynamic characteristics analysis. The vibration absorption mechanism of the vibration absorption system is studied. For instance, Eq. (1) is used to calculate a response surface as follows.

2. Methods and materials

2.1 The structure of TBM-tuned mass vibration absorption system

The TBM main system consists of a cutterhead main drive system and a propulsion system. Cutterhead main drive system is driven by multiple motors synchronously to provide rotary motion for the cutterhead, the propulsion system provide axial motion by the main propulsion cylinder, breaking rocks under the coordination of two movements. The support frame was surrounded by side shields, left-top shield, right-top shield and top shield. The structure and working principle of the shield system were shown in Fig. 1. During the actual excavation process, each shield was supported by the shield

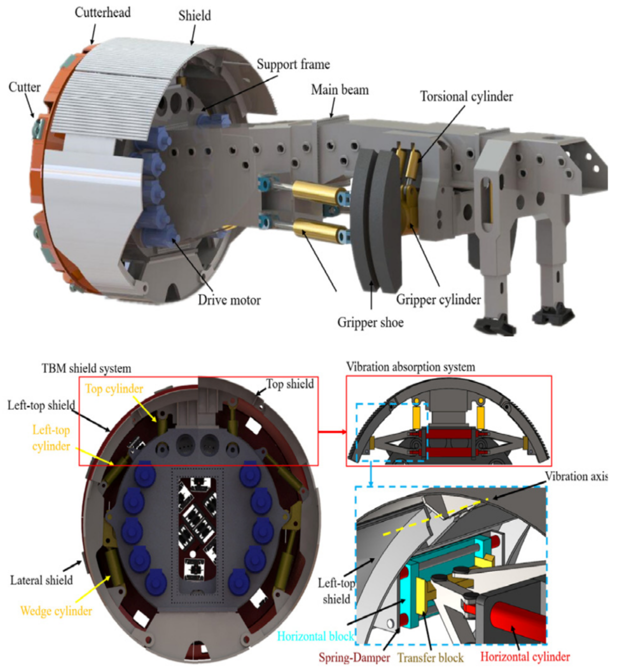

Fig. 1. Main structure of TBM and vibration absorption system.

cylinder against the surrounding rock to provide the radial support for the TBM main system. The shield cylinder was elongated to increase the diameter of the circle formed by the shield to accommodate changes in the diameter of the surrounding rock, as shown in the right half of Fig. 1. The left-top and right-top shields move with the movement of the lateral shield and the top shield to maintain the integrity of the shield system, it did not support the surrounding rock. Therefore, the left-top and right-top shields were considered as the mass of the vibration absorption system, and the structure of tuned mass vibration absorption system for TBM main driving system was designed as shown in the Fig. 1. The system set a horizontal cylinder to adjust the horizontal distance of the left-top and right-top shields to accommodate the opening degree of the shield system. The system used the structure in the Fig. 1 to transmit the axial and overturning vibrations of the system to the horizontal and axial vibration of the transfer block. There was a horizontal wedge connection between the force transfer block and the horizontal block, so that only the axial vibration of the transfer block was transmitted to the horizontal block right-top shield and left-top shield. The upper left and upper right shields were axially reciprocating vibration under the influence of two sets of spring damping systems with the movement of the horizontal block. By adjusting the natural frequency of the vibration absorption system, the system absorbed the vibration energy of TBM main system to the greatest extent.

It can be seen from Fig. 2(a) that in the case of axial vibration, the horizontal blocks on the left and right sides exhibited axial vibration in the same direction with the vibration of the system, thereby driving the left-top and right-top shields to reciprocate axially in the same direction. It can be seen from Fig. 2(b) that in the case of horizontal overturning vibration, the left and right horizontal blocks vibrated in the opposite direction with the vibration of the system, thereby driving the left-top and right-top shields to reciprocate in the opposite direction. Through the above structural relationship, the system realized the coordination of the axial vibration and the the overturning vibration of the system.

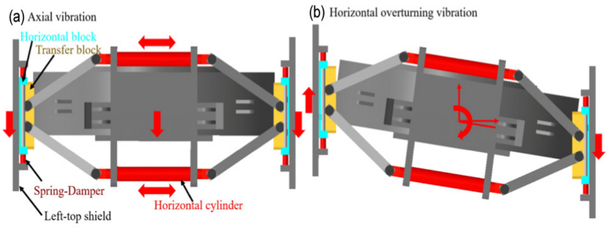

Fig. 2. Vibration coordination relationship of vibration absorption system.

2.2 The dynamic model for TBM main system and TMVAS

(1) The dynamic model for TBM main system

Based on the multi-source driving mode, support mode and structural form of the TBM main system, the multi-degree-of-freedom coupling dynamics model of the TBM main system was established as shown in Fig. 3. The system's axial, vertical, horizontal translational freedom, horizontal, vertical overturning freedom and torsional freedom were considered in the dynamic model.

According to the dynamic model, the dynamic equations of each component were obtained as follows:

For cutterhead:

$$\begin{cases} m_r\ddot{X}_r+\sum_{i=1}^{N}(F_{pri}+D_{pri})\sin(\varphi_i+\alpha)+C_{eqr}(\dot{X}_r-\dot{X}_d)+k_{eqr}(X_r-X_d)=F_X \\ m_r\ddot{Y}_r-\sum_{i=1}^{N}(F_{pri}+D_{pri})\cos(\varphi_i+\alpha)+C_{eqr}(\dot{Y}_r-\dot{Y}_d)+k_{eqr}(Y_r-Y_d)=F_Y \\ m_r\ddot{z}_r=F_z-\sum_{i=1}^{4}[k_{ardi}(z_{ri}-z_{di})+c_{adl1i}(\dot{z}_{ri}-\dot{z}_{di})] \\ I_{rx}\ddot{\theta}_{rx}=M_x+a_r[k_{ard1}(z_{r1}-z_{d1})+c_{ard1}(\dot{z}_{r1}-\dot{z}_{d1}) \\ \qquad -k_{ard3}(z_{r3}-z_{d3})-c_{ard3}(\dot{z}_{r3}-\dot{z}_{d3})] \\ I_{ry}\ddot{\theta}_{ry}=M_y+a_r[k_{ard4}(z_{r4}-z_{d4})+c_{ard4}(\dot{z}_{r4}-\dot{z}_{d4}) \\ \qquad -k_{ard2}(z_{r2}-z_{d2})-c_{ard2}(\dot{z}_{r2}-\dot{z}_{d2})] \\ I_r\ddot{\theta}_r-\sum_{i=1}^{N}(F_{pri}+D_{pri})r_{br}=-T_L . \end{cases}$$

For pinion:

$$\begin{cases} m_{pi}\ddot{X}_{pi}+(F_{pri}+D_{pri})\cos\alpha+C_{eqpi}\dot{\delta}_{dpxi}+k_{eqpi}\delta_{dpxi}=0 \\ m_{pi}\ddot{Y}_{pi}+(F_{pri}+D_{pri})\sin\alpha+C_{eqpi}\dot{\delta}_{dpyi}+k_{eqpi}\delta_{dpyi}=0 \\ I_{mi}\ddot{\theta}_{mi}+C_{mpQ}(\dot{\theta}_{mi}-\dot{\theta}_{pi})+k_{mpQ}(\theta_{mi}-\theta_{pi})=T_{pi} \\ I_{pi}\ddot{\theta}_{pi}+(F_{pri}+D_{pri})r_{bp}+C_{mpQ}(\dot{\theta}_{pi}-\dot{\theta}_{mi})+k_{mpQ}(\theta_{pi}-\theta_{mi})=0. \end{cases}$$

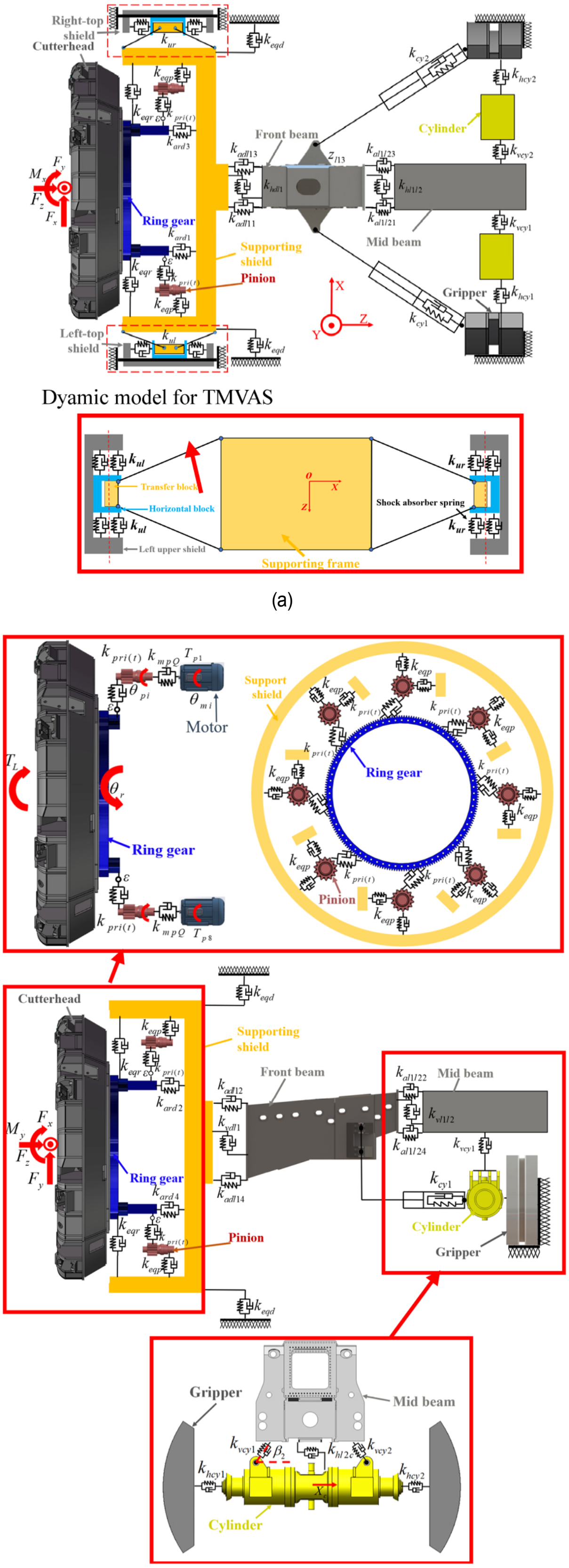

(a)

(b)

Fig. 3. Dynamic model for TBM main system and TMVAS.

For support frame:

$$\left\{\begin{aligned}
&m_d\ddot{X}_d + C_{eqr}(\dot{X}_d-\dot{X}_r) + C_{eqd}\dot{X}_d + k_{eqr}(X_d-X_r) + k_{eqd}X_d + \sum_{i=1}^{8}(C_{eqp}\dot{\delta}_{pdxi} + k_{eqp}\delta_{pdxi})\\
&\qquad +[k_{hdl1}(X_d-X_{l1}) + c_{hdl1}(\dot{X}_d-\dot{X}_{l1})] = 0\\
&m_d\ddot{Y}_d + C_{eqr}(\dot{Y}_d-\dot{Y}_r) + C_{eqd}\dot{Y}_d + k_{eqr}(Y_d-Y_r) + k_{eqd}Y_d + \sum_{i=1}^{8}(C_{eqp}\dot{\delta}_{pdyi} + k_{eqp}\delta_{pdyi})\\
&\qquad +k_{vdl1}(Y_d-Y_{l1}) + c_{vdl1}(\dot{Y}_d-\dot{Y}_{l1})] = 0\\
&m_d\ddot{z}_d = \sum_{i=1}^{4}[k_{ardi}(z_{ri}-z_{di}) + c_{adl1i}(\dot{z}_{ri}-\dot{z}_{di})] - \sum_{i=1}^{4}[k_{adl1i}(z_{di}-z_{l1i}) + c_{adl1i}(\dot{z}_{di}-\dot{z}_{l1i})]\\
&I_{dx}\ddot{\theta}_{dx} = -a_r[k_{ard1}(z_{r1}-z_{d1}) + c_{ard1}(\dot{z}_{r1}-\dot{z}_{d1}) - k_{ard3}(z_{r3}-z_{d3}) - c_{ard3}(\dot{z}_{r3}-\dot{z}_{d3})]\\
&\qquad + a_{l1}[k_{adl11}(z_{d1}-z_{l11}) + c_{adl11}(\dot{z}_{d1}-\dot{z}_{l11}) - k_{adl13}(z_{d3}-z_{l13})\\
&\qquad - c_{adl13}(\dot{z}_{d3}-\dot{z}_{l13})]\text{-}f_l r_d - f_r r_d\\
&I_{dy}\ddot{\theta}_{dy} = -a_r[k_{ard4}(z_{r4}-z_{d4}) + c_{ard4}(\dot{z}_{r4}-\dot{z}_{d4}) - k_{ard2}(z_{r2}-z_{d2}) - c_{ard2}(\dot{z}_{r2}-\dot{z}_{d2})]\\
&\qquad + a_{lq}[k_{adl14}(z_{d4}-z_{l14}) + c_{adl14}(\dot{z}_{d4}-\dot{z}_{l14}) - k_{adl12}(z_{d2}-z_{l12})\\
&\qquad - c_{adl12}(\dot{z}_{d2}-\dot{z}_{l12})]\text{-}f_b r_d - f_a r_d
\end{aligned}\right.$$

For main beam system:

$$\left\{\begin{aligned}
&m_{l1}\ddot{X}_{l1} = [k_{hdl1}(X_d-X_{l1}) + c_{hdl1}(\dot{X}_d-\dot{X}_{l1})]\\
&\qquad -[k_{hl1l2}(X_{l1}-X_{l2}) + c_{hl1l2}(\dot{X}_{l1}-\dot{X}_{l2})]\\
&\qquad -[X_{l1cy1}k_{cy1} + \dot{X}_{l1cy1}c_{cy1}]\cos\beta_1 - [X_{l1cy2}k_{cy2} + \dot{X}_{l1cy2}c_{cy2}]\cos\beta_1\\
&m_{l1}\ddot{Y}_{l1} = k_{vdl1}(Y_d-Y_{l1}) + c_{vdl1}(\dot{Y}_d-\dot{Y}_{l1})] - [k_{vl1l2}(Y_{l1}-Y_{l2}) + c_{vl1l2}(\dot{Y}_{l1}-\dot{Y}_{l2})]\\
&m_{l2}\ddot{X}_{l2} = [k_{hl1l2}(X_{l1}-X_{l2}) + c_{hl1l2}(\dot{X}_{l1}-\dot{X}_{l2})] - (k_{vcy1}\delta_{l2c1} + c_{vcy1}\dot{\delta}_{l2c1})\cos\beta_2\\
&\qquad + (k_{vcy2}\delta_{l2c2} + c_{vcy2}\dot{\delta}_{l2c2})\cos\beta_2 - [k_{h12c}(X_{l2}-X_c) + c_{h12c}(\dot{X}_{l2}-\dot{X}_c)]\\
&m_{l2}\ddot{Y}_{l2} = [k_{vl1l2}(Y_{l1}-Y_{l2}) + c_{vl1l2}(\dot{Y}_{l1}-\dot{Y}_{l2})] - (k_{vcy1}\delta_{l2c1} + c_{vcy1}\dot{\delta}_{l2c1})\sin\beta_2\\
&\qquad - (k_{vcy2}\delta_{l2c2} + c_{vcy2}\dot{\delta}_{l2c2})\sin\beta_2\\
&m_c\ddot{X}_c = [k_{h12c}(X_{l2}-X_c) + c_{h12c}(\dot{X}_{l2}-\dot{X}_c)] - (k_{hcy1}X_c + c_{hcy1}\dot{X}_c)\\
&\qquad - (k_{hcy2}X_c + c_{hcy2}\dot{X}_c) + (k_{vcy1}\delta_{l2c1} + c_{vcy1}\dot{\delta}_{l2c1})\cos\beta_2\\
&\qquad - (k_{vcy2}\delta_{l2c2} + c_{vcy2}\dot{\delta}_{l2c2})\cos\beta_2\\
&m_{l1}\ddot{z}_{l1} = \sum_{i=1}^{4}[k_{adl1i}(z_{di}-z_{l1i}) + c_{adl1i}(\dot{z}_{di}-\dot{z}_{l1i})] - \sum_{i=1}^{4}[k_{al1l2i}z_{l1i} + c_{al1l2i}\dot{z}_{l1i}]\\
&\qquad + [x_{l1cy1}k_{cy1} + \dot{x}_{l1cy1}c_{cy1}]\sin\alpha - [x_{l1cy2}k_{cy2} + \dot{x}_{l1cy2}c_{cy2}]\sin\alpha\\
&I_{l1x}\ddot{\theta}_{l1x} = -a_{l1}[k_{adl11}(z_{d1}-z_{l11}) + c_{adl11}(\dot{z}_{d1}-\dot{z}_{l11}) - k_{adl13}(z_{d3}-z_{l13})\\
&\qquad - c_{adl13}(\dot{z}_{d3}-\dot{z}_{l13})] + a_{l1}[k_{al1l21}z_{l11} + c_{al1l21}\dot{z}_{l11} - k_{al1l23}z_{l13} - c_{al1l23}\dot{z}_{l13}]\\
&\qquad + a_{l1m}[-x_{l1cy1}k_{cy1} - \dot{x}_{l1cy1}c_{cy1} - x_{l1cy2}k_{cy2} - \dot{x}_{l1cy2}c_{cy2}]\\
&I_{l1y}\ddot{\theta}_{l1y} = -a_{lq}[k_{adl14}(z_{d4}-z_{l14}) + c_{adl14}(\dot{z}_{d4}-\dot{z}_{l14}) - k_{adl12}(z_{d2}-z_{l12}) - c_{adl12}(\dot{z}_{d2}-\dot{z}_{l12})]\\
&\qquad + a_{lq}[k_{al1l24}z_{l14} + c_{al1l24}\dot{z}_{l14} - k_{al1l22}z_{l12} - c_{al1l22}\dot{z}_{l12}]\,.
\end{aligned}\right. \tag{1}$$

F_x, F_y, F_z was the horizontal, vertical and axial equivalent loads of the cutterhead; T_{pi} was the output torque of the *i-th* motor; T_L was the equivalent total torque of the cutterhead; M_x,M_y was the horizontal and vertical load of the cutterhead. X_j, Y_j, Z_j, θ_j, θ_{jx}, θ_{jy} represented the horizontal displacement, vertical displacement, axial displacement, torsional displacement, horizontal overturning displacement and vertical overturning displacement of the *j* component. *m, I* indicated the equivalent mass and moment of inertia of each component. $j = r, d, l_1, l_2, c, pi, mi$ represented the cutterhead, the main drive support frame, the front section of the main beam, the middle section of the main beam, the saddle frame, the *i-th* drive gear and the *i-th* drive motor. The stiffness and damping of each key part of the dynamic model were shown in Table 1.

Intermediate variables Z_{ri} (i = 1-4) was the axial displacement of the lower, left, upper, and right positions of the cutterhead; Z_{di} (i = 1-4) was the axial displacement of the lower, left, upper, and right positions of the support frame; Z_{l1i} (i = 1-4) was the axial displacement of the lower, left, upper, and right positions

Table 1. Stiffness and damping in dynamic model.

k_{eqr}	Main bearing radial stiffness
k_{eqp}	Radial supporting stiffness of the pinion
k_{eqd}	Support stiffness of the shield body and the surrounding rock
k_{adl1i}/c_{adl1i} (i = 1-4)	Axial stiffness/damping of the cutterhead system and the front section of the main beam
k_{hdl1}/c_{hdl1}	Horizontal stiffness/damping of the cutterhead system and the front section of the main beam
k_{cy1}/c_{cy1}	Stiffness/damping of left thrust cylinder
k_{hcy1}/c_{hcy1}	Stiffness/damping of left gripper cylinder
k_{Lr}	Torsional stiffness of the cutterhead flange
k_{mpQ}	Torsional stiffness of the gear-connecting shaft
$k_{pri(t)}$	Time-varying meshing stiffness of pinion and gear ring
k_{al1l2i}/c_{al1l2i} (i = 1-4)	Axial stiffness/damping of the front section of the main beam and the middle section of the main beam
k_{hl1l2}/c_{hl1l2}	Horizontal stiffness/damping of the front section of the main beam and the middle section of the main beam
k_{cy2}/c_{cy2}	Stiffness/damping of right thrust cylinder
k_{hcy2}/c_{hcy2}	Stiffness/damping of right gripper cylinder

of the front section of main beam; these intermediate variables can be calculated by Eq. (2).

$$\begin{cases} z_{r1} = z_r - a_r\theta_{rx} \\ z_{r2} = z_r + a_r\theta_{ry} \\ z_{r3} = z_r + a_r\theta_{rx} \\ z_{r4} = z_r - a_r\theta_{ry} \end{cases} \begin{cases} z_{d1} = z_d - a_{l1}\theta_{dx} \\ z_{d2} = z_d + a_{lq}\theta_{dy} \\ z_{d3} = z_d + a_{l1}\theta_{dx} \\ z_{d4} = z_d - a_{lq}\theta_{dy} \end{cases} \begin{cases} z_{l11} = z_{l1} - a_{lq}\theta_{l1x} \\ z_{l12} = z_{l1} + a_{lq}\theta_{l1y} \\ z_{l13} = z_{l1} + a_{lq}\theta_{l1x} \\ z_{l14} = z_{l1} - a_{lq}\theta_{l1y} \end{cases} \tag{2}$$

where a_r was the axial roller radius of the bearing; a_{l1} was half the length of the flange between the support frame and the front section of the main beam; a_{lq} was half the width of the flange between the support frame and the front section of the main beam.

Intermediate variables x_{pri} was the relative deformation between the large ring gear and the pinion, calculated by projecting the displacement of the pinion and the large ring gear along the meshing line, as shown in Eq. (3):

$$x_{pri} = r_{bp}\theta_{pi} - r_{br}\theta_r + Y_{pi}\sin\alpha + X_{pi}\cos\alpha + X_r\sin(\alpha + \varphi_i) - e_{pri}(t) \tag{3}$$

$$\rho_e = \alpha + \varphi_i \tag{4}$$

where u_r, u_{pi} was the relative displacement of the ring gear and pinion along the meshing line; X_r, Y_r, X_{pi}, Y_{pi} was the horizontal and vertical displacement of the large ring gear and the pinion; α, φ_i was the meshing angle and the phase angle of each pinion; r_{br} was the radius of the large ring; r_{bp} was the pinion base circle radius. Considering the relative deformation relationship and the gear clearance, the time-varying meshing force F_{pri} of the gear and the time-varying meshing damping force D_{pri} of the gear can be calculated by the method of Refs. [11, 13].

Intermediate variables x_{l1cy1}, x_{l1cy2} was the relative deformation of the front section of the main beam and the supporting cylinder, calculated by Eq. (5):

$$\begin{cases} x_{l1cy1} = X_{l1}\cos\beta_1 - z_{l1}\sin\beta_1 + a_{l1m}\theta_{l1x} \\ x_{l1cy2} = X_{l1}\cos\beta_1 + z_{l1}\sin\beta_1 + a_{l1m}\theta_{l1x} \end{cases} \tag{5}$$

where β_1 was the support angle of the main propulsion cylinder, and a_{l1m} was the projection distance from the centroid of the front section of the main beam to the support cylinder along the support direction.

Intermediate variables δ_{pdxi}, δ_{pdyi}, δ_{dpxi}, δ_{dpyi} was the relative horizontal and vertical displacement of the i-th pinion and the support frame, δ_{pdxi}, δ_{pdyi} was obtained by the projection of the pinion in the coordinate system of the support frame; δ_{dpxi}, δ_{dpyi} was obtained by the projection of the support frame in the pinion's coordinate system.

$$\begin{cases} \delta_{pdxi} = X_d + Y_{pi}\cos\varphi_i + X_{pi}\sin\varphi_i \\ \delta_{dpxi} = X_{pi} - Y_d\cos\varphi_i + X_d\sin\varphi_i \end{cases} \begin{cases} \delta_{pdyi} = Y_d + Y_{pi}\sin\varphi_i - X_{pi}\cos\varphi_i \\ \delta_{dpyi} = Y_{pi} + Y_d\sin\varphi_i + X_d\cos\varphi_i \end{cases} \tag{6}$$

where X_d,Y_d was horizontal and vertical displacement of the support frame.

Intermediate variables δ_{l2c1}, δ_{l2c2} was the horizontal and vertical relative displacements of the middle section of the main beam and the saddle, the displacement of the middle section of the main beam and the saddle were respectively projected to the anti-torsion cylinder, as shown in the Eq. (7).

$$\begin{cases} \delta_{l2c1} = X_{l2}\cos\beta_2 + Y_{l2}\sin\beta_2 - X_c\cos\beta_2 \\ \delta_{l2c2} = -X_{l2}\cos\beta_2 + Y_{l2}\sin\beta_2 + X_c\cos\beta_2 \end{cases} \tag{7}$$

where X_{l2},Y_{l2},X_c,Y_c was the horizontal and vertical displacement of the middle section of the main beam and the saddle frame, β_1 was the anti-torsion cylinder support angle.

(2) The dynamic model for TBM-TMVAS

Due to the presence of the horizontal block in the TMVAS, the horizontal displacement of the transfer block cannot be transmitted to the left-top and right-top shields. At the same time, the axial and overturning vibration of the support frame was determined by the analysis in Sec. 3.4 as its main vibration form. Therefore, in the TBM-TMVAS dynamics model, the axial DOF and overturning DOF of the support frame, the axial DOF of the left-top and right-top shields were considered.

$$K_r = \frac{1}{2}m_r\dot{z}_r^2 + \frac{1}{2}I_r\dot{\theta}_{rx}^2 \; K_d = \frac{1}{2}m_d\dot{z}_d^2 + \frac{1}{2}I_d\dot{\theta}_{dx}^2 \; K_{ul} = \frac{1}{2}m_{ul}\dot{z}_{ul}^2 \; K_{ur} = \frac{1}{2}m_{ur}\dot{z}_{ur}^2$$

$$K = K_r + K_d + K_{ul} + K_{ur}$$

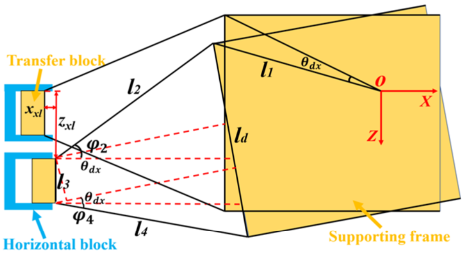

Fig. 4. Translational displacement relationship of the transfer block.

$$
\begin{aligned}
&P_{rd}=\frac{1}{2}k_{ard3}(z_{r3}(z_r,\theta_{rx})-z_{dr3}(z_d,\theta_{dx}))^2+\frac{1}{2}k_{ard1}(z_{r1}(z_r,\theta_{rx})-z_{d1}(z_d,\theta_{dx}))^2\\
&P_{dm}=\frac{1}{2}k_{adl13}(z_{d3}(z_d,\theta_{dx}))^2+\frac{1}{2}k_{adl11}(z_{d1}(z_d,\theta_{dx}))^2\\
&P_u=\frac{1}{2}k_{ur}(z_{xr}(z_d,\theta_{dx})-z_{ur})^2+\frac{1}{2}k_{ul}(z_{xl}(z_d,\theta_{dx})-z_{ul})^2\\
&P=P_{rd}+P_{dm}+P_u\ .
\end{aligned}
\tag{8}
$$

Based on the Lagrange dynamics method, the local dynamic equations of the TMVAS were shown in the equation. The overturning vibration and axial vibration equation of the support frame in Eq. (1) were replaced by following equation, and the vibration equations of the left-top and right-top shields were added to Eq. (9), and the overall dynamic equations of the TMVAS are obtained.

$$
\begin{aligned}
&m_r\ddot{z}_r+(k_{ard3}+k_{ard1})(z_r-z_d)=F_z\\
&I_r\ddot{\theta}_{rx}+(k_{ard3}+k_{ard1})r_d^2\theta_{rx}-(k_{ard3}+k_{ard1})r_m r_d\theta_{dx}=M_x\\
&m_d\ddot{z}_d+(k_{ard3}+k_{ard1})(z_d-z_r)+(k_{adl13}+k_{adl11})z_d\\
&\qquad+k_{ur}(z_{xr}-z_{ur})+k_{ul}(z_{xl}-z_{ul})=0\\
&I_{dx}\ddot{\theta}_{dx}+(k_{ard3}+k_{ard1})r_m^2\theta_{dx}-(k_{ard3}+k_{ard1})r_m r_d\theta_{rx}\\
&\qquad+(k_{adl13}+k_{adl11})r_m^2\theta_{dx}+P_{11}k_{ur}(z_{xr}-z_{ur})\\
&\qquad+P_{21}k_{ul}(x_{xl}-z_{ul})=0\\
&m_{ur}\ddot{z}_{ur}+k_{ur}(z_{ur}-z_{xr})=0\\
&m_{ul}\ddot{z}_{ul}+k_{ul}(z_{ul}-x_{xl})=0
\end{aligned}
\tag{9}
$$

where K_i represented the kinetic energy of the i component and P_i represented the elastic potential energy of the i component. x_{xl}, z_{xl}, x_{xr}, z_{xr} were the horizontal and axial displacement of transfer block on left and right side, they were functions of z_d and θ_{dx}. The functional relationship was obtained by mechanism motion analysis of the TMVAS's structure. The motion relationship of the TMVAS was mainly the motion relationship between the support frame and the transfer block. Assume that the horizontal overturning displacement of the support frame was θ_{dx}, and the horizontal and vertical translational displacement of the transfer block was as shown in the Fig. 4.

When $\theta_{dx} < 0$,φ_{2l},φ_{4l} satisfied the following Eq. (10):

$$
\begin{aligned}
&l_2\sin(\varphi_{2l}-|\theta_{dx}|)+l_4\sin(\varphi_{4l}+|\theta_{dx}|)+l_3\cos(|\theta_{dx}|)=l_d\\
&l_2\cos(\varphi_{2l}-|\theta_{dx}|)+l_3\sin(|\theta_{dx}|)=l_4\cos(\varphi_{4l}+|\theta_{dx}|)
\end{aligned}
\tag{10}
$$

where l_1 was the distance from the first hinge to the center of mass of the support frame, l_2, l_4 was the length of the connecting rod, l_3 was the distance between the two hinges of the transfer block. The angle between the two connecting rods on the right and the horizontal line φ_{2r}, φ_{4r} were as follows:

$$
\varphi_{2l}=\varphi_{4r}\quad \varphi_{4l}=\varphi_{2r}\ .
\tag{11}
$$

The horizontal overturning vibration of the support frame was converted into the horizontal and axial displacement of the transfer block by the link structure. The corresponding displacement x_{xl}, z_{xl}, x_{xr}, z_{xr} was calculated by following Eq. (12):

$$
\begin{aligned}
&x_{xl}=l_1\cos(\varphi_{sf})+l_2\cos(\varphi_{2l\_origin})-[l_1\cos(\varphi_{sf}-|\theta_{dx}|)+l_2\cos(\varphi_{2l})]\\
&z_{xl}=l_2\sin(\varphi_{2l})-l_1\sin(\varphi_{sf}-|\theta_{dx}|)-[l_2\sin(\varphi_{2l\_origin})-l_1\sin(\varphi_{sf})]+z_d\\
&x_{xr}=l_1\cos(\varphi_{sf}+|\theta_{dx}|)+l_2\cos(\varphi_{2r})-[l_1\cos(\varphi_{sf})+l_2\cos(\varphi_{2r\_origin})]\\
&z_{xr}=l_2\sin(\varphi_{2r})-l_1\sin(\varphi_{sf}+|\theta_{dx}|)-[l_2\sin(\varphi_{2r\_origin})-l_1\sin(\varphi_{sf})]+z_d\ .
\end{aligned}
\tag{12}
$$

When $\theta_{dx} > 0$, φ_{2r}, φ_{4r} satisfied the following Eq. (13):

$$
\begin{aligned}
&l_2\sin(\varphi_{2r}-|\theta_{dx}|)+l_4\sin(\varphi_{4r}+|\theta_{dx}|)+l_3\cos(|\theta_{dx}|)=l_d\\
&l_2\cos(\varphi_{2r}-|\theta_{dx}|)+l_3\sin(|\theta_{dx}|)=l_4\cos(\varphi_{4r}+|\theta_{dx}|)\ .
\end{aligned}
\tag{13}
$$

The angle between the two connecting rods on the left and the horizontal line φ_{2l}, φ_{4l} were as follows:

$$
\varphi_{2l}=\varphi_{4r}\quad \varphi_{4l}=\varphi_{2r}\ .
\tag{14}
$$

Horizontal and axial displacement of the left and right transfer block x_{xl}, z_{xl}, x_{xr}, z_{xr}, were calculated by Eq. (15):

$$
\begin{aligned}
&x_{xr}=-l_1\cos(\varphi_{sf})-l_2\cos(\varphi_{2r\_origin})+[l_1\cos(\varphi_{sf}-|\theta_{dx}|)+l_2\cos(\varphi_{2r})]\\
&z_{xr}=l_2\sin(\varphi_{2r})-l_1\sin(\varphi_{sf}-|\theta_{dx}|)-[l_2\sin(\varphi_{2r\_origin})-l_1\sin(\varphi_{sf})]+z_d\\
&x_{xl}=-l_1\cos(\varphi_{sf}+|\theta_{dx}|)-l_2\cos(\varphi_{2l})+[l_1\cos(\varphi_{sf})+l_2\cos(\varphi_{2l\_origin})]\\
&z_{xl}=l_2\sin(\varphi_{2l})-l_1\sin(\varphi_{sf}+|\theta_{dx}|)-[l_2\sin(\varphi_{2l\_origin})-l_1\sin(\varphi_{sf})]+z_d\ .
\end{aligned}
\tag{15}
$$

The dynamic differential equations of the above TBM system and TMVAS were combined and expressed in matrix form, which can be expressed as follows:

$$
\boldsymbol{M}\ddot{\boldsymbol{X}}+\boldsymbol{C}\dot{\boldsymbol{X}}+\boldsymbol{K}\boldsymbol{X}=\boldsymbol{F}
\tag{16}
$$

where M was the system mass matrix; C and K were the damping matrix and stiffness matrix, respectively; F was the external excitation force vector; X was the displacement vector. The dynamic response of the system was calculated by using the above dynamic model, and the dynamic model was solved by Newmark-β method [25, 26].

2.3 Calculation method of equivalent load of cutter head

The cutter group breaking rock load was combined on the cutterhead face to form the equivalent load of the cutterhead, which was the external excitation of the TBM to cause extreme vibration. Wherein, the lateral force of the cutter and the rolling force synthesized the radial unbalanced load of the cutterhead, which caused radial vibration of the TBM system; the vertical force of the cutter formed the axial load of the cutter head; the vertical force of the cutter on the respective pole diameters formed TBM overturning moment, which caused the TBM's overturning vibration. The rolling force of the cutter on the respective pole diameters formed torque load of TBM which caused the torsional vibration. The three-direction load data segments of each cutter were randomly intercepted during the process of synthesizing the cutterhead load to simulate the random rock breaking process of different cutters. At the same time, the three-direction force was modified according to the Refs. [27, 28] to simulate the variation of the three-direction load of different cutters at different polar diameters. Finally, the time-varying characteristics of the cutter phase angle at each position was considered to meet the requirements of the cutterhead rotation characteristics. The equivalent axial force F_L, radial unbalance force F_X, F_Y, overturning moment M_X, M_Y and torque T_L of the cutterhead were calculated according to the Eq. (17).

$$\begin{aligned}
F_Z &= \sum_{i=1}^{n} Rand(F_{Ni})\eta_i + \sum_{j=1}^{p}(Rand(F_{Nj}) + Rand(F_{sj})\sin\beta_j) \\
F_X &= \sum_{i=1}^{n} Rand(F_{si})\cos(\omega t+\theta_i)\mu_i + \sum_{i=1}^{n} Rand(F_{ri})\sin(\omega t+\theta_i)\xi_i \\
&\quad + \sum_{j=1}^{p} Rand(F_{rj})\sin(\omega t+\theta_j) + \sum_{j=1}^{p} Rand(F_{si})\cos(\beta_j)\cos(\omega t+\theta_j) \\
F_Y &= \sum_{i=1}^{n} Rand(F_{si})\sin(\omega t+\theta_i)\mu_i + \sum_{i=1}^{n} Rand(F_{ri})\cos(\omega t+\theta_i)\xi_i \\
&\quad + \sum_{j=1}^{p} Rand(F_{rj})\cos(\omega t+\theta_j) + \sum_{j=1}^{p} Rand(F_{si})\cos(\beta_j)\sin(\omega t+\theta_j) \\
M_X &= \sum_{i=1}^{n} Rand(F_{Ni})\rho_i\cos(\omega t+\theta_i)\eta_i \\
&\quad + \sum_{j=1}^{p}(Rand(F_{Nj}) + Rand(F_{sj})\sin\beta_j)\rho_j\cos(\omega t+\theta_j) \\
M_Y &= \sum_{i=1}^{n} Rand(F_{Ni})\rho_i\sin(\omega t+\theta_i)\eta_i \\
&\quad + \sum_{j=1}^{p}(Rand(F_{Nj}) + Rand(F_{sj})\sin\beta_j)\rho_j\sin(\omega t+\theta_j) \\
T_L &= \sum_{i=1}^{n} Rand(F_{ri})\rho_i\xi_i + \sum_{j=1}^{p} Rand(F_{rj})\rho_j \,.
\end{aligned} \tag{17}$$

The subscript i was the i_{th} center cutter and inner cutter, and the subscript j indicated the j_{th} cutter side cutter. F_N, F_s and F_r represented the vertical, lateral and rolling force of cutter; θ represented the polar angle of the cutter; ρ represented the diameter of the cutter; β indicated the installing angle of the cutter; Rand represented random data segments from a specific load spectrum; ω was the rotational angular velocity of the cutter head; t was the simulation time; η_i, ξ_i, μ_i was the correction coefficient of the vertical force, lateral force and rolling force of the *i-th* cutter in the direction of the polar diameter [6].

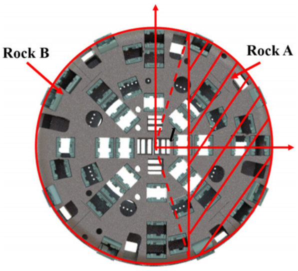

Fig. 5. Schematic diagram of soft-hard rock intersecting face.

For continuous tunneling conditions, the surrounding rock conditions are often complex and uncertain, and it is difficult to accurately describe the complete tunnel rock conditions with a certain function. In the actual tunneling process, in addition to uniform geological conditions with different rock resistance, the surrounding rock types mainly include composite geological conditions with different rock proportions. When the surrounding rock condition is complex surrounding rock, the cutter load of the cutter head needs to be changed according to different rock areas. It is assumed that the complex surrounding rock area is shown as Fig. 5. There are two types of rocks on the turning face, A and B. When the *kth* cutter is in the tunneling face area of rock A during the rotation of the cutter head, the rock breaking load of the cutter changes to the corresponding a rock breaking load. During calculation, assuming that the total thrust of the TBM tunneling remains unchanged, the equivalent axial force $F_{Z\text{-AB}}$ of the cutter head in the case of complex geology satisfies the Eq. (18).

$$\begin{aligned}
F_{Z\text{-AB}} = F_{Z\text{-B}} = \sum_{i=1}^{n} Rand(F_{Ni})\eta_i\mu_i + \\
\sum_{j=1}^{p}(Rand(F_{Nj})\mu_j + Rand(F_{sj})\mu_j\sin\beta_j)
\end{aligned} \tag{18}$$

where μ_i and μj is cutter's additional load factor under type B rock.

Therefore, in the process of synthesizing the cutter head's equivalent load, it is necessary to determine which rock area each cutter is at in real time. The three-way load of the *i-th* cutter is shown in Eq. (19):

$$\begin{aligned}
F_{si} &= \begin{cases} F_{si-B} & \rho_i\cos(\omega t+\theta_i) < l \\ F_{si-A} & \rho_i\cos(\omega t+\theta_i) > l \end{cases} \\
F_{ri} &= \begin{cases} F_{ri-B} & \rho_i\cos(\omega t+\theta_i) < l \\ F_{ri-A} & \rho_i\cos(\omega t+\theta_i) > l \end{cases} \\
F_{Ni} &= \begin{cases} F_{Ni-B} & \rho_i\cos(\omega t+\theta_i) < l \\ F_{Ni-A} & \rho_i\cos(\omega t+\theta_i) > l \end{cases}
\end{aligned} \tag{19}$$

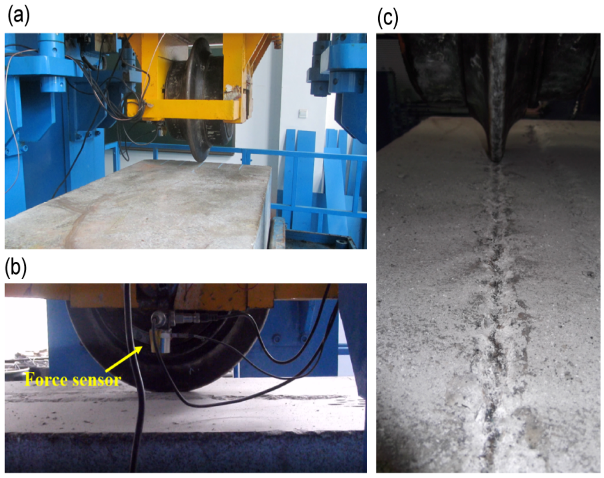

Fig. 6. Rock breaking experiment.

where $F_{Ni\text{-}B}$, $F_{si\text{-}B}$ and $F_{ri\text{-}B}$ represent the dynamic normal force, side force and rolling force between the *i-th* cutter and the B type rock respectively; $F_{Ni\text{-}A}$, $F_{si\text{-}A}$ and $F_{ri\text{-}A}$ represent the dynamic normal force, side force and rolling force between the *i-th* cutter and the A type rock respectively; l is the horizontal distance from the interface of a rock to the cutter head's center.

2.4 Cutter-rock breaking test method

The cutter-rock breaking experiment was based on the reciprocating TBM cutter linear cutting test bench in Central South University, as shown in Fig. 6(a). The test bench had a size of 5 m × 3.2 m × 3.5 m and a bearing capacity of 60 t, which can be used for cutter straight cutting experiments. The size of the rock sample was 1000 mm × 500 mm × 300 mm. A three-direction force sensor was placed on the cutter shaft to test the three-direction load generated during the rock breaking process, as shown in Fig. 6(b). Therefore, the load of the inner hob was obtained through experiments, and the rock-breaking load spectrum of the side cutter was simulated by LYS-DYNA, according to the Refs. [27, 28].

2.5 Field vibration test method

In order to modify the dynamic model, verify the accuracy of the dynamic response of the system, and determine the vibration frequency band of the main structure, based on a water diversion project, the vibration of the TBM support frame, main beam and the gripper cylinder were measured which was shown in the Fig. 7. The acceleration sensor was capable of testing the three-way vibration data at the test point, and the sampling frequency was 1000 Hz. During the field test, the compressive strength of the rock was 80-120 MPa, the speed of the cutterhead was about 5-6 rpm, and the penetration degree was 5-6 mm, so as to ensure the rock characteristics and rock breaking condition were consistent with the rock breaking experiment.

Table 2. Statistics of TBM actual tunneling parameter.

Tunneling parameter	Value	Tunneling parameter	Value
Advance force (kN)	1.3608e4	Top cylinder pressure (bar)	84.4706
Torque (kN.m)	2.6983e3	Advance cylinder pressure (bar)	137.1961
Shield cylinder pressure (bar)	93.0654	Wedge cylinder (bar)	78.6993
Torque cylinder pressure (bar)	95.6144	Gripper cylinder pressure (bar)	257.8366
Rotate speed of cutterhead (Rpm)	5.6	Cutterhead penetration (mm)	5

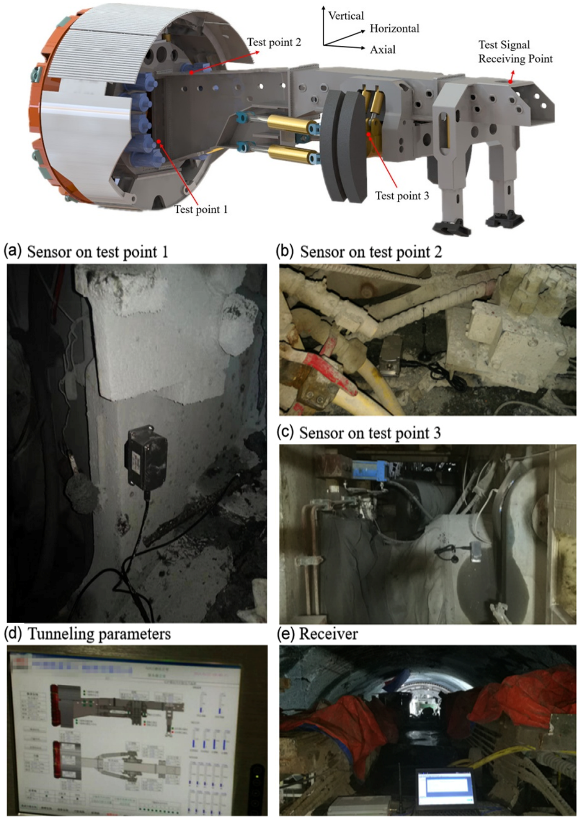

(a) Sensor on test point 1
(b) Sensor on test point 2
(c) Sensor on test point 3
(d) Tunneling parameters
(e) Receiver

Fig. 7. Acceleration field test.

3. Results and discussion

3.1 Main parameters of the dynamic model

In order to ensure the accuracy of the calculation, the main parameters of the dynamic model are calculated by using the TBM actual excavation parameters corresponding to the vibration measurement process of a water diversion project. During the excavation process, the TBM torque and the pressure of each major support cylinder of the system are shown in the Fig. 8. The main statistical values are shown in the Table 2.

According to the hydraulic cylinder pressure parameters in the Table 2, the equivalent stiffness of each support cylinder was calculated according to the Eqs. (17) and (18). The results

Table 3. Main equivalent stiffness in dynamic model.

Stiffness	Value	Stiffness	Value
k_{cy1} / k_{cy2} (N/m)	4.5e8	k_{hcy1} / k_{hcy2} (N/m)	1.2e9
k_{eqdt} (N/m)	3.05e8	K_{vcy1} / k_{vcy2} (N/m)	1.5e8
k_{eqdc} (N/m)	3.55e8		

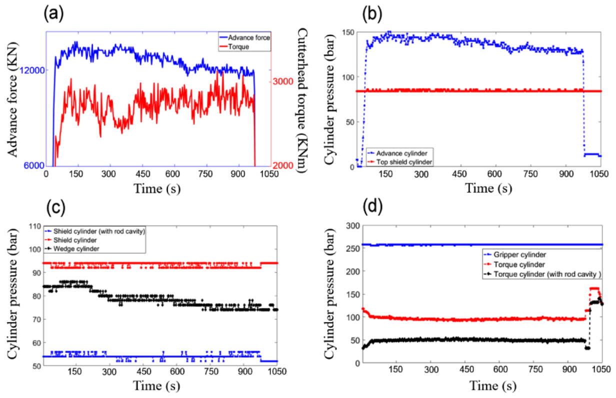

Fig. 8. TBM actual tunneling parameters.

are shown in Table 3.

3.2 Calculation of system equivalent external load

(1) The load on cutters

The equivalent load of the cutterhead is synthesized by the rock breaking load of each cutter. In the calculation process of the cutterhead load, the load of inner cutters were obtained from the cutter-rock breaking experiment, and the load of side cutters were calculated by numerical simulation. The gneiss with rock compressive strength of 60-70 Mpa, granite with rock compressive strength of about 95-100 MPa and 120-130 Mpa were selected as the rock sample. The penetration degree of the cutter in the experiment was 5.39 mm, and the penetration of the excavation parameters was 5 mm. The experiment tested the dynamic three-direction load of the cutter during rock breaking process by the sensor installed in the cutter shaft. The sampling frequency of the experiment process was 225 Hz. The three-dimensional measured loads of the cutter under three rock resistance are shown in Figs. 9(a), (d) and (g), respectively. The frequency domain analysis of the cutter load spectrum is performed. The rolling force frequency domain of the cutter under different rock resistance are shown in Figs. 9(b), (e) and (h), and the frequency domain diagrams of the normal and side forces of the cutter are shown in Figs. 9(c), (f) and (i).

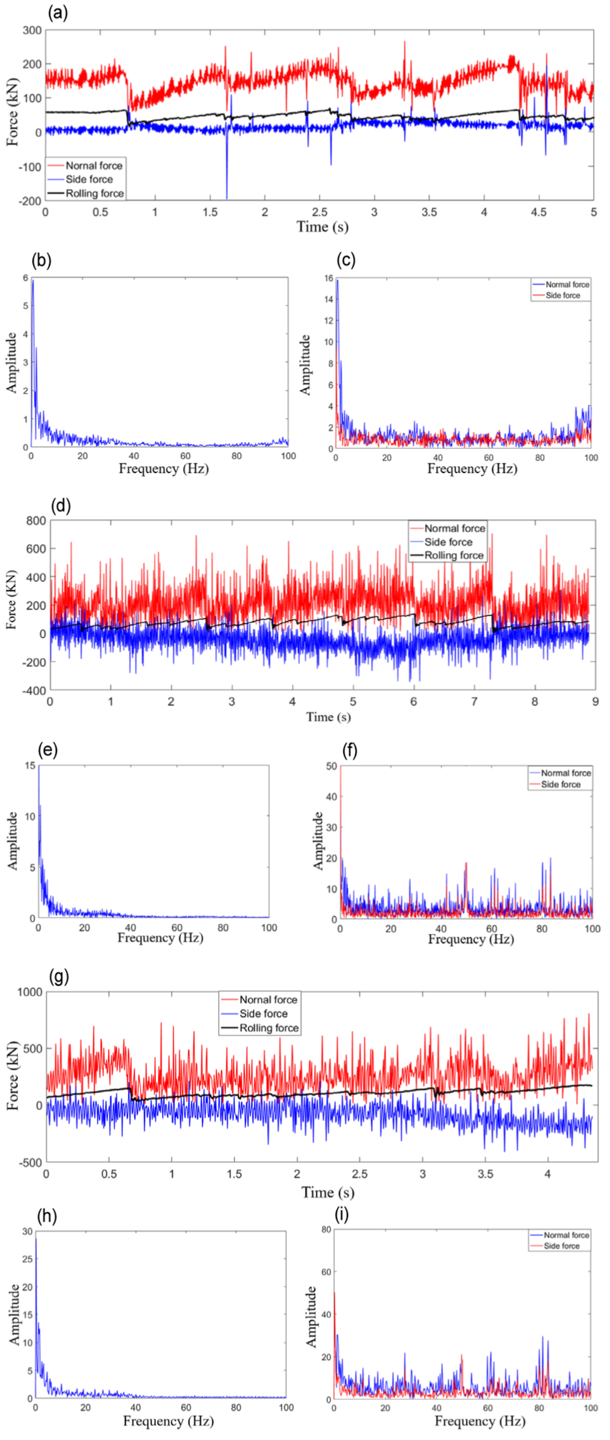

Fig. 9. Time domain and frequency domain signal of cutter load.

It can be seen that as the resistance of the rock increases, the fluctuations of the normal force, rolling force and side force of the cutter increase significantly. It can be seen from the frequency domain analysis of the dynamic load of the cutter under various rock resistance that the frequency domain characteristics are relatively close. The frequency domain of the rolling force is focus in 0-5 Hz, and the frequency response of the normal and side force is not only focus on low-frequency composition below 5 Hz, it also exhibits a wide-band composition in the frequency domain of 100 Hz. At the same time, when the rock resistance is low, it shows a more uniform characteristic in its wide frequency band, and when the rock resistance in-

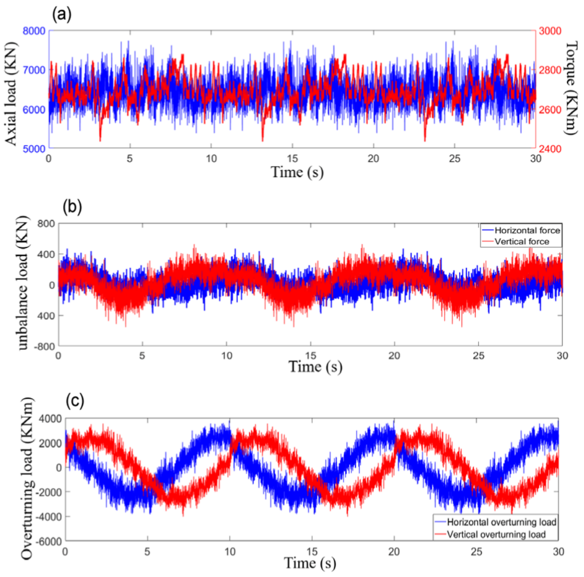

Fig. 10. The external excitation load of cutterhead.

creases, its frequency response shows a higher peak at 15 Hz, 25 Hz, 40 Hz, 50 Hz, etc. As the rock resistance increases, this peak value becomes more significant, but the overall frequency response still maintains a significant broadband characteristic. According to the synthetic law of the cutter head load, the equivalent torque of the cutter head is mainly superimposed by the rolling force of the cutter, while the axial force, overturning moment and radial unbalanced force are superimposed by the cutter's normal force and side force. The main vibration forms of the TBM main system are axial vibration and overturning vibration, which are caused by the overturning moment and axial force. Therefore, according to the above analysis, the overturning moment and the axial force of the system under different rock resistance both exhibit wide-band frequency response characteristics within 100 Hz.

(2) Equivalent load on cutterhead

After obtaining the three-direction force of the cutters which was close to the rock breaking condition in real tunneling progress, take the rock with 100 MPa compressive strength as an example, the equivalent load of the cutterhead was calculated according to the calculation method in Sec. 2.4, and the external excitation load of the cutterhead is as shown in the Fig. 10.

3.3 System modal analysis

TMVAS can mainly reduce the horizontal overturning vibration and axial vibration of the system. In order to explore the vibration mechanism of the system's overturning vibration and axial vibration, the system was modally analyzed. The first 6 modes of the system and the corresponding mode of vibration were shown in the Table 4.

Table 4. The first 6 natural frequency of the cutterhead system.

Natural frequency /Hz	Vibration form
ω1 = 15.3	Translational vibration mode (vertical direction)
ω2 = 16.6	Overturning vibration mode (vertical direction) Translational vibration mode (axial direction)
ω3 = 17.4	Translational vibration mode (horizontal direction)
ω4 = 18.2	Overturning vibration mode (horizontal direction) Translational vibration mode (axial direction)
ω5 = 29.2	Translational vibration mode (vertical direction)
ω6 = 39.0	Translational vibration mode (axial direction)

From the Table 4, it can be seen that the first-order mode of vibration was the vertical translational vibration of the system, which indicated that the vertical equivalent stiffness of the TBM main system was the smallest. The second-order mode of vibration was a coupled vibration of the vertical overturning vibration and the axial translational vibration.

The third-order mode of vibration was a horizontal translational vibration of the system. The fourth-order mode of vibration was the coupled vibration of the system's horizontal overturning vibration and axial translational vibration. At the same time, the natural frequencies corresponding to the first four modes were close to each other, and were between 15-18 Hz. Therefore, the first four orders of vibration are prone to coupling between modes. According to the measured data of the axial vibration of the system in Sec. 3.5, the main frequency range of the axial vibration of the system was between 15-20 Hz. Therefore, the main vibration of the system during the actual tunneling process was a coupled vibration of its first to fourth mode vibration mode.

3.4 The main vibrational energy of the system under external excitation

In order to study the main forms of system vibration under typical excavation conditions, the vibration energy of each degree of the system was calculated. The horizontal, vertical, axial translational vibration (HYV, VTV, ATV) and horizontal and vertical overturning vibration (HOV, VOV) energy of the support frame were shown in Table 5 and Fig. 11.

The vibration energy of the main drive support frame in all directions was as shown. The vibration energy values in all directions were normalized. It can be seen from the figure that in the vibration of the supporting frame, the HOV accounts for 32.49 % of the total vibration energy; the VOV and the ATV were relatively smaller, accounting for 24.73 % and 24.33 % of the total vibration energy, respectively; the HTV and VTV account for the smallest proportion (less than 10 %) of the total energy of the system vibration. Therefore, the main vibration energy of the main drive system under the impact load of the cutter head was mainly the overturning vibration and the axial translational vibration. The TBM multi-DOF TMVAS proposed in this paper was mainly aimed at reducing the axial and horizontal overturning vibration of the system, it met the actual vibration reduction requirements of the system during the actual tunneling process.

Table 5. Vibration statistics of each degree of freedom.

Vibration energy proportion	HOV	VOV	ATV	HTV	VTV
Support frame	32.49 %	24.73 %	24.33 %	9.80 %	8.67 %

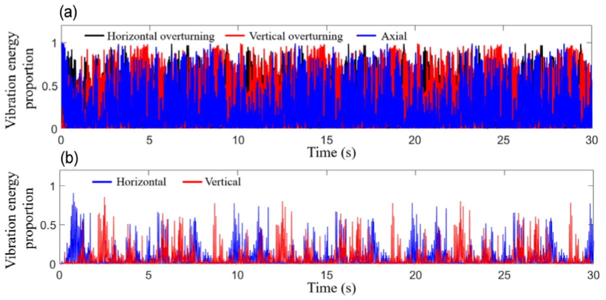

Fig. 11. Vibration energy of each degree of freedom.

3.5 Main vibration response analysis of the system

In order to accurately determine the vibration of the system under the conditions of excavation, the main dynamic parameters of the system are corrected according to the vibration data and the accuracy of the dynamic model was improved. At the same time, in order to determine the main vibration frequency of TBM main support frame, the corresponding frequency domain analysis were carried out as shown in Fig. 12.

It can be seen from the Fig. 12 that among the acceleration of the support frame and the main beam, the axial acceleration is the largest, the lateral acceleration was the second, and the longitudinal acceleration is the smallest. When the vibration was transmitted to the gripper cylinder, the vibration amplitude was already small, and the three-direction acceleration RMS values were all below 0.06 g.

At the same time, the time domain response calculated by the modified dynamic model was close to the test result. The calculation error of the horizontal and vertical acceleration of the support frame is about 26 %, and the calculation error of the axial acceleration was about 8 %. The calculation error of the three-direction acceleration at the main beam was controlled within 25 %; the calculation error of the horizontal acceleration at the gripper cylinder was within 8 %. Hence, the dynamic model modified based on the measured data has high calculation accuracy and can accurately calculate the vibration of the TBM main system. At the same time, the main frequencies of the support frame's axial vibration data were concentrated at 15-25 Hz, 30 Hz, 55-60 Hz, 75-85 Hz. The main frequencies of the axial vibration data of the support frame calculated by the dynamic model were concentrated in the frequency bands of 15-20 Hz, 20-30 Hz, 42 Hz, 50 Hz, 60 Hz. The frequency distribution of the system vibration calculated by the dynamic model agreed well with the measured data. The main frequency segments coincided in the 15-20 Hz segment, which indicated that the model can accurately describe the actual vibration of the system from the frequency domain.

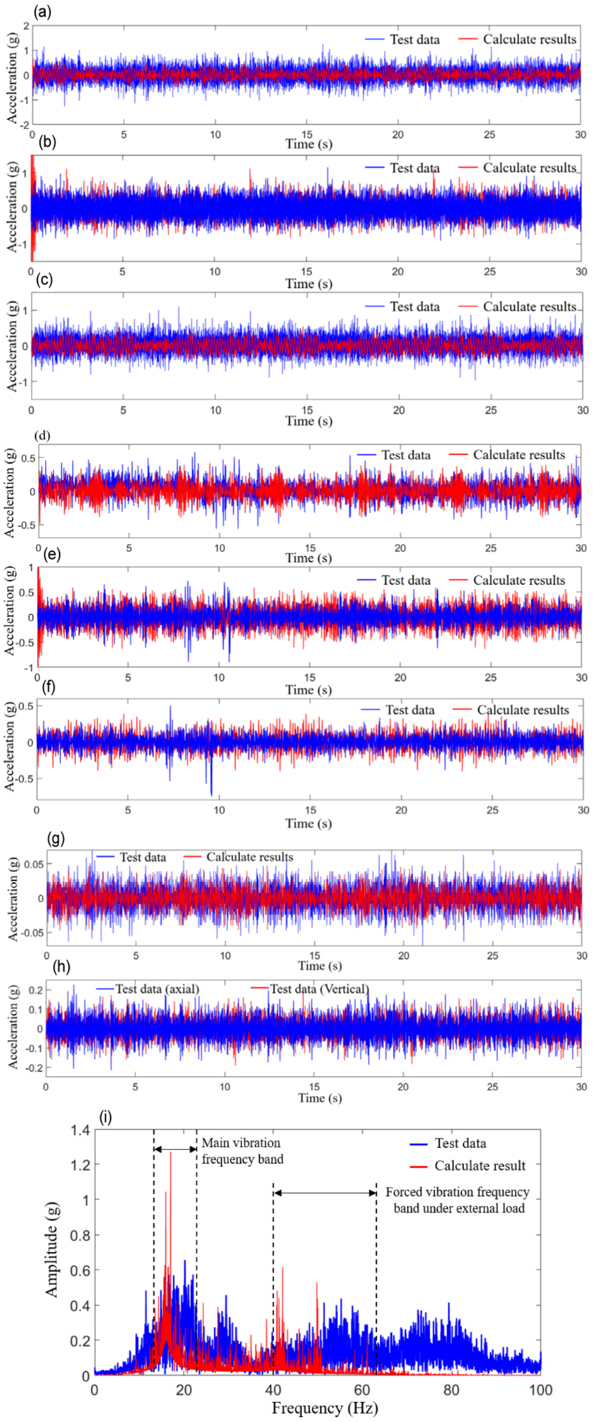

Fig. 12. Test and calculate acceleration response of TBM main system: (a) horizontal acceleration on supporting frame; (b) axial acceleration on supporting frame; (c) vertical acceleration on supporting frame; (d) horizontal acceleration on main beam; (e) axial acceleration on main beam; (f) vertical acceleration on main beam; (g) horizontal acceleration on gripper cylinder; (h) axial and vertical acceleration on gripper cylinder; (i) frequency domain responses of axial acceleration on supporting frame.

This provides the basis for the design of TMVAS. In the figure, the frequency domain components of the 42 Hz, 50 Hz,

Table 6. Test and calculate acceleration response statistics.

	Support frame		
	Horizontal	Vertical	Axial
Calculate	0.173	0.160	0.302
Test	0.234	0.218	0.279
Error	26.55 %	26.59 %	8.24 %
	Main beam		
	Horizontal	Vertical	Axial
Calculate	0.126	0.211	0.120
Test	0.137	0.170	0.096
Error	8.11 %	23.7 %	25.81 %
	Gripper cylinder		
	Horizontal	Vertical	Axial
Calculate	-	0.015	-
Test	0.047	0.016	0.056
Error	-	7.64 %	-

and 60 Hz of the main frame were identical to the corresponding frequency components in the cutter's load. Therefore, these frequency components were forced vibrations due to the excitation of the cutterhead. The 15-20 Hz frequency band was a coupled vibration of its first to fourth mode vibration mode according to the modal analysis in Sec. 3.3. Since the low frequency vibration in the range of 12-20 Hz accounted for the largest proportion of the axial vibration of the support frame, this frequency band was the main frequency band considered in the design of the TMVAS. In Ref. [15], the axial acceleration of the bottom of the main beam was tested based on the TBM real tunneling progress. The test result showed that the main vibration frequency was around 14 Hz, which was basically consistent with the results of this paper.

3.6 Optimization of main parameters of TMVAS

The maximum value of the horizontal overturning vibration and the axial vibration of the support frame was optimized for the stiffness and damping ratio of TMVAS. The optimization history of the stiffness and damping parameters were shown in the Fig. 13. When the stiffness value was below 5.9e7 N/m, the axial and horizontal overturning vibration amplitude of the support frame was significantly reduced as the stiffness value increases. When the stiffness value was about 5.9e7 N/m, the axial vibration amplitude of the support frame was the smallest and the horizontal overturning vibration amplitude was at a low level. When the stiffness of the TMVAS was greater than the stiffness, as the value of the stiffness increased, the amplitude of the support frame increased gradually. At the same time, when the system damping ratio was around 0.029, the maximum amplitudes of axial vibration and overturning vibration were at a low level. Therefore, it can be determined that the optimal stiffness for TMVAS was about 5.9e7 N/m, and the optimal damping ratio was around 0.029.

Table 7. Acceleration response statistics of the support frame and the cutterhead.

Support frame	HOV	HOV (with TMVAS)	ATV	ATV (with TMVAS)
RMS	0.7776	0.7204	2.9644	2.7133
Amplitude	2.2289	1.9388	10.9307	8.0128
Cutterhead	HOV	HOV (with TMVAS)	ATV	ATV (with TMVAS)
RMS	0.5968	0.6151	4.2547	3.9595
Amplitude	2.1688	2.0656	14.9069	11.4446

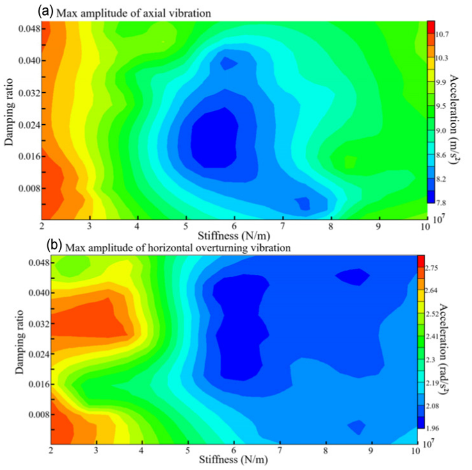

Fig. 13. The optimization history of the stiffness and damping parameters.

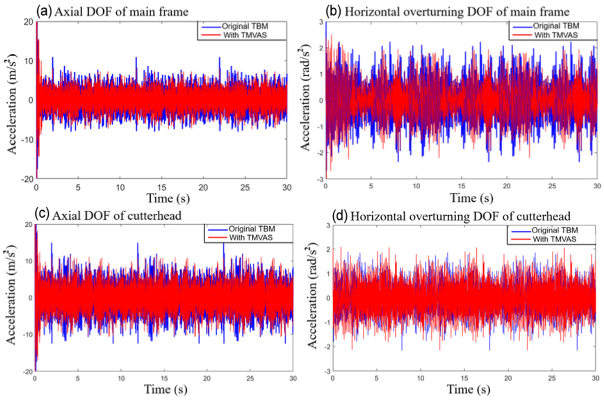

Fig. 14. Acceleration of main components of TBM.

3.7 Vibration absorption effect of TMVAS

The main component acceleration response of the original TBM system and the TBM system containing the TMVAS were extracted and compared as shown in Fig. 14.

The axial and overturning direction acceleration response statistics of the support frame and the cutterhead are shown in the Table 7.

It can be seen from the Fig. 14 that under the action of the TMVAS, the vibration in the axial direction and the horizontal overturning direction of the TBM support frame was signifi-

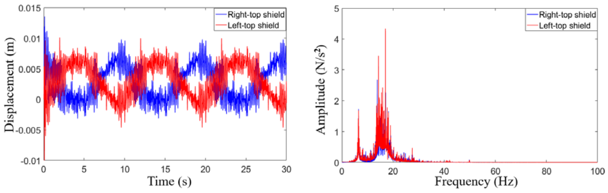

Fig. 15. The displacement response of the mass blocks.

cantly reduced. The RMS of the axial acceleration was reduced by 9.3 %, and the amplitude was reduced by 26.7 %. The RMS of the horizontal overturning direction acceleration was reduced by 7.4 %, and the amplitude was reduced by 13.0 %.

Due to the reduced vibration of the support frame, the vibration of the cutter head was indirectly reduced. The system did not significantly reduce the vibration of the horizontal overturning vibration of the cutterhead. The vibration RMS and the maximum amplitude differed by about 3 %. TMVAS played a more significant role in reducing the axial vibration of the cutter head, and its maximum amplitude was reduced by 23.2 %.

The mass blocks continued to vibrate during the TBM excavation process to absorb the vibration energy of the system. In order to verify the vibration mechanism of the designed TMVAS, the displacement response of the mass blocks were extracted and analyzed in the frequency domain as shown in the Fig. 15.

It can be seen that the right-top shield and the left-top shield periodically vibrate with periodic changes of the overturning load, the vibration amplitude was around 5 mm. The vibrational displacement of the right-top shield and the left-top shield was opposite, which was consistent with the motion characteristics of the TMVAS's structure. Under the reverse synchronous motion of the two mass blocks, the resulting dynamic axial force and overturning moment counteracted the dynamic load at the support frame, thereby reducing the vibration of the support frame. It can be seen from the frequency domain analysis of the vibration displacement of the two mass blocks that the main vibration frequency was between 10-20 Hz. The stiffness value of the TMVAS was 5.9e7 N/m, and the natural frequency can be calculated to be 16.9 Hz. From the field test data and the calculation of dynamic model, it can be seen that the main frequency band of the system vibration frequency of the support frame was 10-20 Hz. Therefore, the TMVAS will resonates under the vibration of the TBM main system, so that the two mass blocks will absorb the maximum vibration energy, thereby minimizing the axial and overturning vibration of the system.

3.8 The effect of mass blocks

The above analysis maintained the mass of the mass blocks, in order to study the effect of the mass of the mass blocks on the vibration absorption effect, additional mass of 0.5, 1, 1.5 times of the mass block was added to the original mass block.

Table 8. The vibration absorption statistics under different additional mass.

Additional mass factor	Case	Stiffness	Damping ratio	Axal/amplitude reduction percentage	Overturning/ amplitude reduction percentage
0.5	Case 1	9.163e7	0.0439	8.072/26.15 %	1.840/17.45 %
	Case 2	1.022e8	0.0418	9.150/16.29 %	1.712/23.19 %
	Case 3	9.694e7	0.0469	8.322/23.87 %	1.776/20.32 %
1.0	Case 1	1.729e8	0.0898	8.395/23.20 %	1.458/34.59 %
	Case 2	2.059e8	0.098	9.0395/17.30 %	1.376/38.37 %
	Case 3	1.876e8	0.0796	8.680/20.59 %	1.426/26.02 %
1.5	Case 1	1.98e8	0.0816	8.397/23.18 %	1.244/44.19 %
	Case 2	2.102e8	0.0959	8.4176/22.99 %	1.235/44.59 %
	Case 3	2.041e8	0.0898	8.4033/23.12 %	1.239/44.41 %

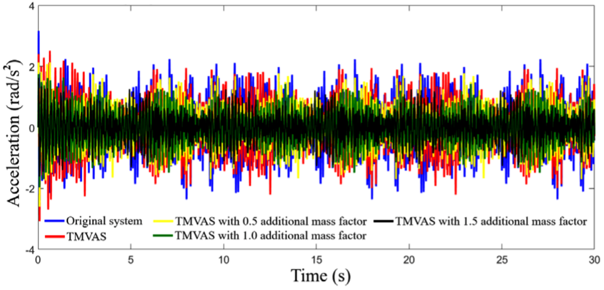
(a) Overturning degree

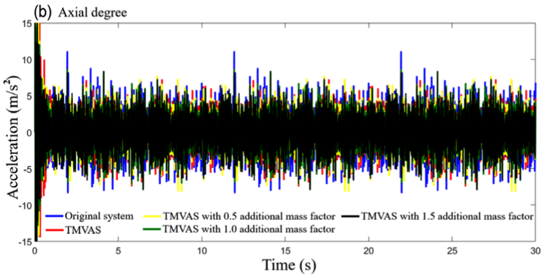
(b) Axial degree

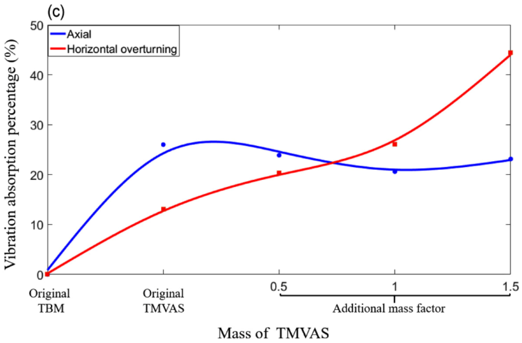

Fig. 16. The vibration absorption effect of the TMVAS under different additional mass.

The stiffness and damping ratio of the system was optimized under different additional mass. The vibration absorption percentage of the TMVAS under different additional mass was shown in Fig. 16 and Table 8.

The percentage of vibration absorption in the overturning direction was significantly improved, and the vibration absorption percentage in the overturning direction was about 13 % without additional mass, and with an additional mass of 0.5, 1, 1.5 times the mass of mass block, the percentage of vibration absorption in the overturning direction was 20 %, 26 % and 44 %, respectively. At the same time, as the mass of the mass block increased, the optimal stiffness increased gradually. Under different condition of additional mass, the natural frequency of the damping system was maintained between 15-20 Hz. This ensured the resonance state of the TMVAS, thereby absorbing the vibration energy of the system at the most.

3.9 Characteristic analysis of TMVAS under continuous driving condition

Under the condition of TBM continuous tunneling, the change of rock conditions mainly includes homogeneous surrounding rock with different hardness and composite surrounding rock with different properties. Therefore, the vibration characteristics of the main system under the above typical rock conditions and the vibration reduction effect of TMVAS were further studied.

The above study has proved that the designed TMVAS has a good damping effect on the vibration of the TBM main system was mainly in the 15-20 Hz frequency band. In order to study the effect of different resistance rocks on the system's main vibration frequency section, taking the load spectrum of cutter under different rock resistance as the equivalent load of the system, the axial load frequency of the vibration-damped part of the main system under different rock resistance was calculated. The response is shown as Fig. 17.

It can be seen from the Fig. 17 that the axial vibration frequency response of the main system's vibration under different rock resistance has a similar rule, and the maximum peak values of vibration under soft, medium and hard rock conditions are 15.9, 17.1 and 18.08 Hz, respectively. There are lower frequency peaks at 40 Hz, 45 Hz, 65 Hz. At the same time, as the rock resistance increases, the frequency components of the system increase significantly.

Therefore, for the system's axial and overturning load under different rock resistance, the main vibration frequency band of the connection part of the TBM supporting frame and the front section of main beam changes little, which are all concentrated in the range of 15-20 Hz. For external excitation loads with significant specific frequency peaks, the system's vibration frequency response is prone to corresponding frequency characteristics and exhibits more prominent forced vibration characteristics. When the external excitation frequency increases, the system's vibration frequency may change. However, since the axial and overturning external excitation loads of the cutterhead under different rock resistance show wide-band frequency characteristics, it is not appropriate to use the system's frequency-response analysis to analyze the corresponding response. It can be seen from the above calculation and analysis that under the external excitation with wide frequency response characteristics, the vibration of this part does not simply show the characteristics of forced vibration, and its vibration frequency is mainly determined by the natural frequencies of the system's 1-4 orders.

Therefore, different rock resistance will not significantly change the main frequency band of the vibration. According to the vibration-damping principle of the TMVAS system, the vibration-damping system designed in this paper can play an effective role in reducing vibration.

In order to study the influence of the different rock properties on the main system's vibration characteristics under the complex geological situation, the corresponding load of the cutter head is calculated which is shown in the following Table 9. The horizontal unbalanced load, torque and axial load change with the proportion of soft surrounding rock as shown in Fig. 18.

As shown in Table 9 and Fig. 18, as the proportion of soft surrounding rock increases, the lateral unbalanced load and torque of the cutter head increase significantly. As the proportion of soft surrounding rock increases, the corresponding load increase rate increases significantly. When the proportion of

Table 9. Statistical value of cutterhead load under different geological conditions.

Rock proportion	0 %	21.3 %	35.2 %	50 %
Horizontal overturning load (KNm)	312.15	325.53	377.74	486.70
Horizontal unbalanced load (KN)	117.48	128.81	161.92	209.22
Cutterhead torque (KNm)	2.8722e3	2.9757e3	3.2662e3	4.2312e3
Load additional factor $\mu_i\mu_j$	1	1.0738	1.2438	1.805

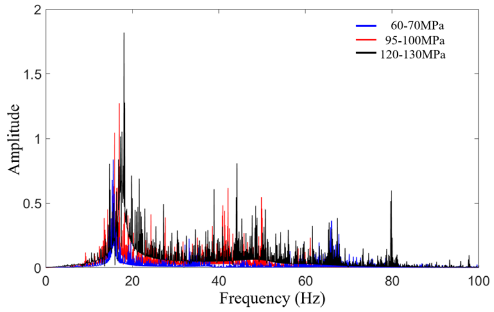

Fig. 17. The vibration frequency response under different resistance rocks.

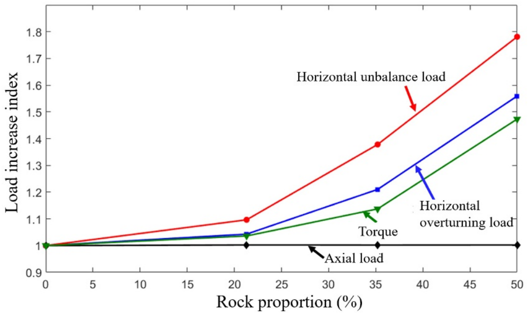

Fig. 18. Load change of cutterhead under different complex geological conditions.

Table 10. Statistical value of damping effect under different geological conditions.

	HOV				ATV			
Rock proportion	0 %	21.3 %	35.2 %	50 %	0 %	21.3 %	35.2 %	50 %
RMS	0.7776	0.8496	0.8899	1.2233	2.9644	3.2631	3.3227	3.8872
Vibration reduction rate	7.4 %	9.3 %	8.4 %	12.6 %	9.3 %	10.1 %	9.9 %	14.1 %
Amplitude	2.2289	2.1840	2.4185	3.8650	10.9307	10.5357	9.9950	12.5687

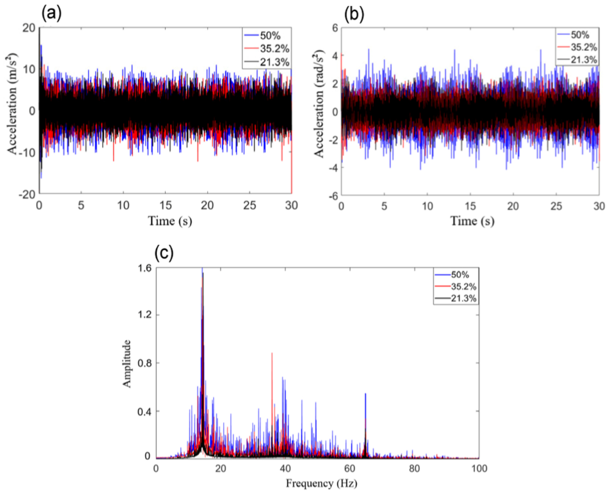

Fig. 19. The vibration frequency response under different rocks proportion.

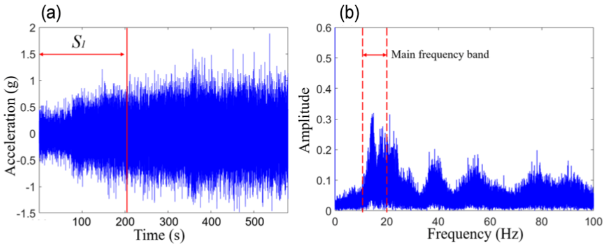

Fig. 20. The time and frequency response under real continuous tunneling conditions with rock property changes significantly.

soft surrounding rock increased to 20 %, the rms value of cutterhead's horizontal overturning load, horizontal unbalanced load and torque increased by 4.29 %, 9.64 % and 3.60 %, respectively. When the proportion of soft surrounding rock increases from 35 % to 50 %, cutterhead's horizontal overturning load, horizontal unbalanced load and torque increased by 28.85 %, 29.21 % and 29.55 %, respectively.

Using the corresponding cutter head's equivalent load under complex geological situation with different rock proportions as the external excitation load of the model, the axial and horizontal overturning vibrations of the supporting frame in each case are calculated as Fig. 19.

The statistical values of the axial and overturning vibration calculation values of the supporting shell under the complex geology of different rock proportions, the statistical values of the damping effect of the TMVAS system on the RMS value and amplitude of the system are Table 10.

As can be seen from the Fig. 19 and Table 10, as the proportion of soft rock increases, the RMS values of the axial and horizontal overturning vibration of the supporting shell increase significantly. Similar to the load change law of the system under different surrounding rock proportions, the increase rate of the system's vibration response increases slowly when the rock proportion is 0-35 %, and the axial vibration RMS value increases by 14.4 %. The rate is 0.4091 % per one percent. The RMS value of the horizontal overturning vibration is increased by 12.1 %, and the increase rate is 0.3438 % per one percent. While the rock proportion is 35 %-50 %, the vibration increase rate is faster, the increase rate of the RMS value of axial vibration reaches 2.8970 % per one percent.

The increase rate of its RMS value of horizontal overturning vibration reaches 1.2867 % per one percent. The change law of the horizontal overturning vibration's amplitude of the supporting shell is consistent with its RMS value. It increases slightly when the proportion of rock is 0-35 %, and the increase value is about 8.5 %. When the proportion of rock is 35-50 %, the increase is larger, which is about 64.9 %. The axial vibration amplitude shows a small fluctuation in the range of 10 % when the rock proportion is 0-35 %, and it increases significantly when the rock proportion is 35-50 %, with an 23.5 % increase amplitude.

At the same time, under complex geological conditions with different proportions of soft surrounding rock, the frequency response of the system's axial vibration is relatively consistent, and its main frequency bands are around 15-20 Hz. The proportion of surrounding rock changes significantly. According to the calculation and comparison of the TMVAS dynamic model analysis, it can be seen that the rock proportion is in the range of 0-35 %. The TMVAS has the same damping effect on the axial vibration and the horizontal overturning vibration, and the damping effect on the system RMS is, respectively, 7 %-9 % and 9 %-10 %. When the soft surrounding rock proportion is large, the system's horizontal overturning vibration increases significantly, the effect of TMVAS on the system's RMS value is significantly increased, which is 12.6 % and 14.1 %, respectively. The maximum damping amplitude for the system is increased to 18.7 % and 29.8 %, respectively.

In order to verify the dynamic characteristics of the main system under continuous tunneling conditions, the continuous vibration test of the main system support shell was conducted for up to 10 minutes under specific tunneling conditions. The rocks are staggered, and the proportion of rocks with different properties changes significantly along the direction of excavation. It can be determined by analyzing the slag on the belt conveyor. The vibration data of the system in the test segment is shown in the Fig. 20, and the frequency domain response corresponding to the S1 data segment is shown in Fig. 20.

Under such tunneling conditions where the rock property changes significantly, the vibration amplitude of the system changes significantly. Taking the S1 segment as an example, the maximum amplitude of acceleration increases more than one time. The frequency response corresponding to the S1 data segment shows that the main frequency range of system vibration remains between 15-20 Hz.

Therefore, the test verifies that the main vibration frequency range of the TBM main system under continuous tunneling conditions, especially when the surrounding rock properties change significantly, remains basically unchanged.

4. Conclusions

In this paper, a design method of tuned mass vibration absorption system was introduced. Through the study of the dynamic characteristics of the main system, it was found that the overturning vibration and axial vibration of the system were the main vibration forms of the system under the excavation condition, and the vibration energy percentage accounted for more than 80 %. Based on the actual excavation process, the vibration data, and the main tunneling parameters and geological parameters during the excavation process were obtained. The above data was used to calculate the main support stiffness of the system, modify dynamic model and verifies the multi-point vibration response of the system. At the same time, it was determined that the axial vibration of the main support frame of TBM was concentrated in the frequency bands of 15-20 Hz, wherein the low frequency vibration of 15-20 Hz was a coupled vibration of its first to fourth mode vibration mode according to the modal analysis. The maximum value of overturning vibration and axial vibration was taken as the optimization target, the optimal stiffness of TMVAS was determined to be about 5.9e7 N/m, and the optimal damping ratio was around 0.029. Through the vibration absorption effect of the TMVAS, the axial and horizontal overturning acceleration of the system support frame was significantly reduced, the maximum amplitude was reduced by 26.7 % and 13 %, respectively, and the vibration RMS value was reduced by up to 9.3 %. Meanwhile, the TMVAS indirectly had a significant vibration absorption effect on the axial vibration of the cutterhead, and its maximum amplitude was reduced by 23.2 %. With the increase of the additional mass of the mass blocks, the axial vibration absorption effect on the support frame did not change significantly, and the vibration absorption percentage was basically maintained between 20 % and 25 %. Under continuous driving conditions, when the resistance of the surrounding rock changes and the proportion of the surrounding rock of different properties changes, the main vibration frequency band of the main system is basically stable, consistent with the first 4 natural frequencies, the TMVAS system has good damping effect. Through the multi-degree-of-freedom tuned mass vibration absorption theory under the random mutation load of the system, the main vibration energy of the system can be effectively reduced based on the existing TBM main structure.

Acknowledgments

The study was funded by National Natural Science Foundation of China (Grant No. 51875076), National Key Research and Development Project (2018YFB1306701), NSFC-Liaoning United Key fund (Grant No. U1708255).

Conflict of Interests

The authors declare that they have no competing interests.

Nomenclature

F : Load
T : Torque
M : Moment
X : Horizontal displacement
Y : Vertical displacement
Z : Axial displacement
θ : Torsional displacement
m : Mass
I : Inertia
k : Stiffness
c : Damping
α : Meshing angle of each pinion
φ : Phase angle of each pinion
r : Radius of the large ring
D : Damping force
β : Angle
δ : Relative displacement of the i-th pinion
K : Kinetic energy
P : Elastic potential energy
l : Length
φ : Angle
ρ : Diameter
β : Installing angle
ω : Rotational angular velocity
t : Time
η : Correction coefficient
ξ : Correction coefficient
μ : Correction coefficient

References

[1] J. Rostami, Hard rock TBM cutterhead modeling for design and performance prediction, *Geomechanik Und Tunnelbau*, 1 (1) (2008) 18-28.

[2] M. Entacher, S. Lorenz and R. Galler, Tunnel boring machine performance prediction with scaled rock cutting tests, *International Journal of Rock Mechanics & Mining Sciences*, 70 (9) (2014) 450-459.

[3] L. Lin et al., Experimental study of specific matching characteristics of tunnel boring machine cutter ring properties and rock, *Wear*, 378-379 (2017) 1-10.

[4] Q. Tan et al., Influence of joint characteristics on rock fragmentation induced by TBM disc cutter, *Journal of Central South*

University, 44 (10) (2013) 4040-4046.

[5] M. Entacher et al., Cutter force measurement on tunnel boring machines – System design, *Tunnelling & Underground Space Technology Incorporating Trenchless Technology Research*, 31 (2012) 97-106.

[6] M. Entacher, G. Winter and R. Galler, Cutter force measurement on tunnel boring machines – Implementation at Koralm tunnel, *Tunnelling & Underground Space Technology Incorporating Trenchless Technology Research*, 38 (3) (2013) 487-496.

[7] Q. M. Gong, J. Zhao and A. M. Hefny, Numerical simulation of rock fragmentation process induced by two TBM cutters and cutter spacing optimization, *Tunnelling & Underground Space Technology Incorporating Trenchless Technology Research*, 21 (3) (2006) 263-263.

[8] Q. M. Gong, J. Zhao and Y. Y. Jiao, Numerical modelling of the effects of joint orientation on rock fragmentation by TBM cutters, *Tunnelling and Underground Space Technology*, 20 (2) (2005) 183-191.

[9] G. Li et al., Numerical simulation of the rock fragmentation process induced by TBM cutters, *Applied Mechanics & Materials*, 249-250 (2012) 1069-1072.

[10] H. Ma, L. Yin and H. Ji, Numerical study of the effect of confining stress on rock fragmentation by TBM cutters, *International Journal of Rock Mechanics & Mining Sciences*, 48 (6) (2011) 1021-1033.

[11] W. Sun et al., Dynamic characteristics study with multidegree-of-freedom coupling in TBM cutterhead system based on complex factors, *Mathematical Problems in Engineering* (2013) 657-675.

[12] S. Wei et al., Hierarchical modeling method and dynamic characteristics of cutter head driving system in tunneling boring machine, *Tunnelling & Underground Space Technology Incorporating Trenchless Technology Research*, 52 (2016) 99-110.

[13] J. Huo et al., Electromechanical coupling dynamics of TBM main drive system, *Nonlinear Dynamics*, 90 (2) (2017) 1-24.

[14] J. Huo et al., Multi-directional coupling dynamic characteristics analysis of TBM cutterhead system based on tunnelling field test, *Journal of Mechanical Science & Technology*, 29 (8) (2015) 3043-3058.

[15] X. Zou, Z. Hui and M. Yongzhen, Performance evaluation of hard rock TBMs considering operational and rock conditions, *Shock and Vibration*, 2018 (2) (2018) 1-17.

[16] H. Tian et al., Force analysis of an open TBM gripping–thrusting–regripping mechanism, *Mechanism & Machine Theory*, 98 (2016) 101-113.

[17] G. Chen, Y. Yang and T. Huang, Vibration analysis of open TBM gripping-thrusting-regripping mechanism, *Mechanism and Machine Theory*, 2019 (134) (2019) 95-116.

[18] K. Vogiatzis, V. Zafiropoulou and H. Mouzakis, Monitoring and assessing the effects from Metro networks construction on the urban acoustic environment: the athens metro line 3 extension, *Science of the Total Environment*, 639 (2018) 1360.

[19] J. Buckley, Monitoring the vibration response of a tunnel boring machine: application to real time boulder detection, *Doctoral Dissertation*, Colorado School of Mines (2015).

[20] X. Tong, X. Zhao and S. Zhao, Load reduction of a monopile wind turbine tower using optimal tuned mass dampers, *International Journal of Control* (2015) 1-31.

[21] K. K. F. Wong, Seismic energy dissipation of inelastic structures with tuned mass dampers, *Journal of Engineering Mechanics*, 135 (4) (2008) 265-275.

[22] H. Yamaguchi and N. Harnpornchai, Fundamental characteristics of multiple tuned mass dampers for suppressing harmonically forced oscillations, *Earthquake Engineering & Structural Dynamics*, 22 (1) (2010) 51-62.

[23] N. Yang, C. M. Wang and T. Balendra, Composite mass dampers for vibration control of wind-excited towers, *Journal of Sound & Vibration*, 213 (2) (1998) 301-316.

[24] R. Rana and T. T. Soong, Parametric study and simplified design of tuned mass dampers, *Engineering Structures*, 20 (3) (1998) 193-204.

[25] H. N. Özgüven and D. R. Houser, Mathematical models used in gear dynamics - a review, *Journal of Sound & Vibration*, 121 (3) (1988) 383-411.

[26] L. Walha, T. Fakhfakh and M. Haddar, Nonlinear dynamics of a two-stage gear system with mesh stiffness fluctuation, bearing flexibility and backlash, *Mechanism & Machine Theory,* 44 (5) (2009) 1058-1069.

[27] J. Huo et al., Simulation and optimization design of three-dimensional rotating cutting action of TBM cutter group with different modes, *Journal of Harbin Engineering University*, 35 (11) (2014) 1403-1408.

[28] Q. Tan et al., Numerical study on mode of breaking rock by TBM cutter in two cutting orders, *Journal of Central South University*, 43 (3) (2012) 940-946.

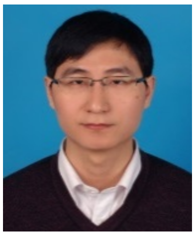

Junzhou Huo now works at Dalian University of Technology. His current research interests include mechanical dynamics, optimal design and mechanical structure life prediction.

Hanyang Wu received master degree in Mechanical Engineering from Dalian University of Technology, Dalian, China, in 2016. His current research interests include mechanical dynamics and mechanical optimal design.

Wenbo Ji now works at Dalian University of Technology. His current research interests include mechanical dynamics and mechanical optimal design.